Nanoscale

ROYAL SOCIETY OF CHEMISTRY

PAPER

View Article Online
View Journal | View Issue

Check for updates

Cite this: *Nanoscale*, 2025, **17**, 22235

A rapid extended-gate field-effect transistor-type biosensor composed of a truncated DNA aptamer and UiO-66 metal–organic framework nanoparticles for HPIV detection in bronchoalveolar lavage fluid

Siyun Lee,[a] Nayeon Kwon,[a] Yejin Yoon,[a] Jinho Yoon,[b] Jong Geol Jang,[c] Wonhwa Lee,*[d,e] Jin-Ho Lee,*[f] Chulhwan Park*[a] and Taek Lee *[a]

The human parainfluenza virus (HPIV), an RNA virus similar to SARS-CoV-2, is a leading cause of both upper and lower respiratory diseases, with potentially fatal outcomes. Thus, early diagnosis of HPIV is crucial. However, current HPIV diagnostic methods face certain limitations. Here, we developed a rapid extended-gate field-effect transistor (R-EGFET)-based biosensor consisting of an HPIV aptamer and UiO-66 metal–organic framework (MOF) nanoparticles, which are capable of rapid and specific detection of HPIV. We synthesized an aptamer that selectively detects HPIV hemagglutinin-neuraminidase (HN protein) using systematic evolution of ligands by the exponential enrichment (SELEX) method. Then, the truncation process was achieved to reduce the aptamer production cost. In addition, the UiO-66 MOF nanoparticle is suitable as a biosensor due to its enhanced electrical sensitivity. The R-EGFET was selected as the detection platform because of its compact design, low cost, and high sensitivity. In addition, incorporating alternating-current electrothermal flow (ACEF) technology reduced the target binding time to 10 min, enabling rapid detection. Thereby, HPIV was detected based on electrical signal changes across the extended-gate membrane using Au microelectrodes. The limit of detection (LOD) of the HPIV HN protein was 22.254 fM in buffer and 36.202 fM in human serum. In clinically relevant samples, the sensor achieved LODs of 9.961 PFU per mL in artificial saliva and 15.273 PFU per mL in bronchoalveolar lavage fluid (BALF), highlighting its potential for practical diagnostic applications. Owing to its rapid detection and high selectivity, the proposed biosensor is expected to be useful for the clinical diagnosis of HPIV.

Received 13th May 2025,
Accepted 22nd August 2025

DOI: 10.1039/d5nr01979f

rsc.li/nanoscale

Published on 23 d'agost 2025. Downloaded on 7/2/2026 16:13:18.

Introduction

Human parainfluenza virus (HPIV) causes acute respiratory infections (ARI) and is a major contributor of upper respiratory tract infections (URTI) and lower respiratory tract infections (LRTI).[1–3] HPIV is an RNA virus belonging to the family *Paramyxoviridae*[4,5] and is classified into four major types based on their antigens (HPIV-1, HPIV-2, HPIV-3 and HPIV-4). HPIV-1 and HPIV-2 are the primary causes of croup in children, and HPIV-3 is more likely to cause severe respiratory disease.[6,7] Globally, HPIV is the second leading cause of acute respiratory disease hospitalization in children under 5 years of age following respiratory syncytial virus (RSV).[8,9] In the United States, approximately 18 000 children are hospitalized each year for LRTI caused by HPIV-3.[10] During the COVID-19 pandemic, the incidence of other respiratory viruses declined. However, an unusual increase in RSV cases in 2021 highlights the need for continued vigilance regarding the spread of respiratory viruses.[11]

In most cases, HPIV infection in healthy adults causes mild symptoms. In contrast, individuals with weakened immune systems, such as children and the elderly, are at higher risk of severe or fatal infection.[12–14] HPIV can cause symptoms, from

[a]*Department of Chemical Engineering, Kwangwoon University, 20 Gwangwoon-Ro, Nowon-Gu, Seoul 01897, Republic of Korea. E-mail: chpark@kw.ac.kr, tlee@kw.ac.kr*
[b]*Department of Biomedical-Chemical Engineering, The Catholic University of Korea, 43 Jibong-ro, Wonmi-gu, Bucheon-si, Gyeonggi-do, 14662, Republic of Korea*
[c]*Division of Pulmonology and Allergy, Department of Internal Medicine, Yeungnam University Medical Center, Yeungnam University College of Medicine, Daegu, Republic of Korea*
[d]*Department of Chemistry, Sungkyunkwan University, Suwon 16419, Republic of Korea. E-mail: wonhwalee@skku.edu*
[e]*Department of MetaBioHealth, Institute for ICS, Sungkyunkwan University, Suwon 16419, Republic of Korea*
[f]*School of Biomedical Convergence Engineering, Pusan National University, Yangsan 50612, Republic of Korea. E-mail: leejh@pusan.ac.kr*

Published on 23 d'agost 2025. Downloaded on 7/2/2026 16:13:18.

cough, runny nose, and fever to more severe respiratory diseases such as bronchitis, pneumonia, and laryngitis.[15,16] Moreover, it can exacerbate pre-existing chronic respiratory conditions such as asthma, making treatment more challenging.[17] However, there are currently no commercially available antiviral agents or vaccines for HPIV infections, and treatment is limited to symptom management.[18–20] The importance of preventing HPIV infection and early diagnosis has been increasingly emphasized.

HPIV infection begins when the hemagglutinin-neuraminidase (HN protein), which serves as a receptor-binding molecule, attaches to sialic acid residues on the cell surface.[21] When the fusion protein (F protein) is activated by the HN protein, the viral envelope fuses with the host cell membrane, releasing the viral nucleoprotein into the cytoplasm.[22] In this manner, the HPIV HN protein is essential for HPIV to approach the cell, enter it, and initiate infection. Therefore, HPIV HN protein was selected as the target for detection.

Conventional HPIV diagnostic methods include enzyme-linked immunosorbent assay (ELISA), immunofluorescence assay (IFA), and reverse transcription polymerase chain reaction (RT-PCR).[23] ELISA and IFA, both serological diagnostics, are widely used because of their high sensitivity for effectively detecting antibodies specific to certain viruses.[24] However, the time required for antibody production hinders early diagnosis of infection, and its high cost remains a significant drawback. In addition, cross-reactive immune responses to certain antigens or antibodies can lead to false-positive results, thereby reducing the specificity of the diagnosis.[25] RT-PCR is an effective method for viral diagnosis due to its high sensitivity, specificity, and rapid results; however, its application is limited by substantial expense and the need for specialized expertise.[26] Thus, we aimed to develop a novel biosensing platform based on an extended-gate field-effect transistor (EGFET) to enable the specific and rapid detection of HPIV.

A field-effect transistor (FET) is one of the most promising platforms for the electrical detection of various biomolecules.[27] The activity of charged biomolecules under physiological conditions contributes to changes in the electrical properties of the membrane and has high sensitivity and specificity, making them effective for biological analysis. In recent years, FET-based aptasensors have attracted considerable attention. Aptamers, owing to their structural tunability, high binding affinity, and excellent stability, can be integrated into FET sensors to enable the sensitive and selective detection of low-concentration biomarkers even in complex biological samples.[28,29] Aptamer-functionalized FET biosensors have been successfully applied to the detection of various targets, including SARS-CoV-2,[30] neurotransmitters,[31,32] inflammatory biomarkers,[33] and other disease-related biomarkers.[34–37] Given these advantages, an aptamer-based EGFET platform was employed in this work. In an EGFET, the transistor is physically separated from the sensing membrane, where chemical reactions occur, allowing for the characterization and operation of the transistor without direct contact with the sample.[38,39] The EGFET sensor, which has the advantages of miniaturization, simple layout, low cost, small sample volume, and long-term stability, is well suited for the on-site detection of HPIV.[40,41]

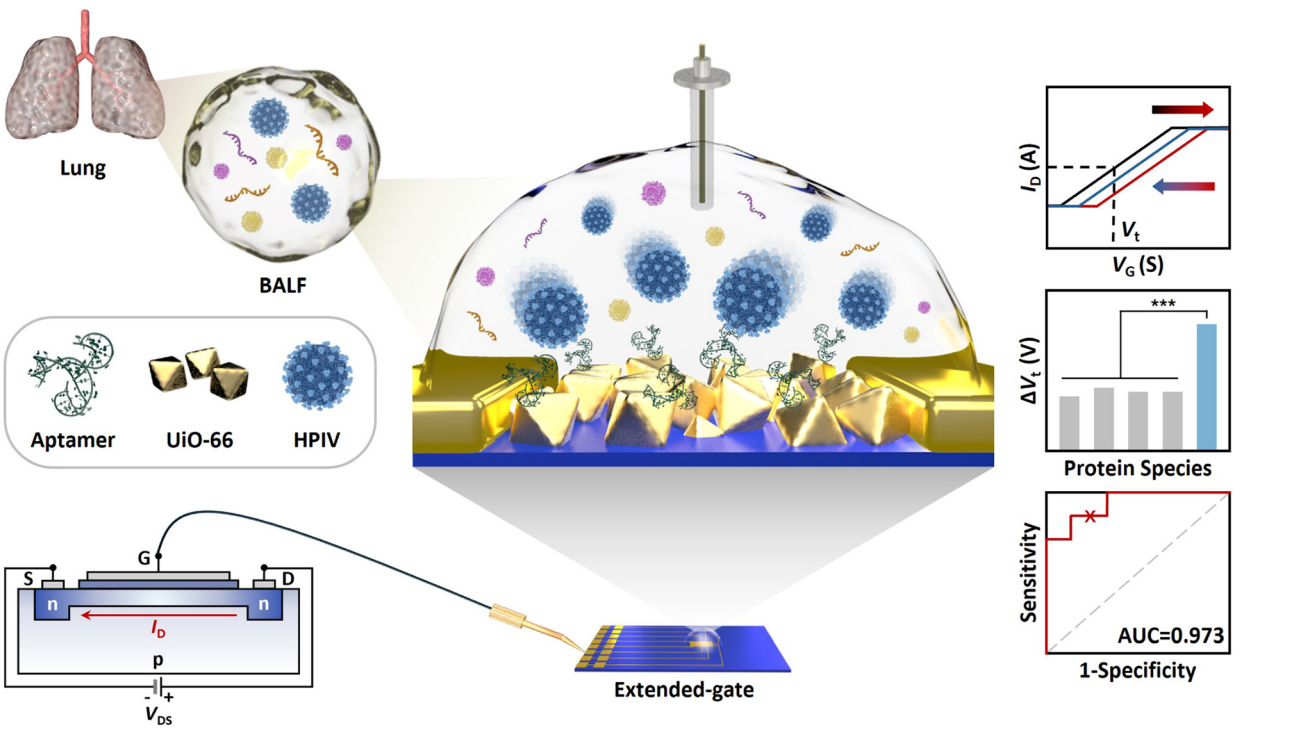

Fig. 1 Schematic illustration of the rapid EGFET biosensing platform for detecting HPIV with an UiO-66 MOF nanoparticle and HPIV aptamer.

This journal is © The Royal Society of Chemistry 2025

Published on 23 d'agost 2025. Downloaded on 7/2/2026 16:13:18.

Recently, metal–organic frameworks (MOFs) have been extensively explored for virus detection. The high porosity, large surface area, and tunable structures make MOFs excellent candidates for biosensing applications. MOFs have been applied in biosensors designed to detect various viruses, including SARS-CoV-2 and dengue virus.[42–46] Zr-based MOFs, with their high porosity and chemical stability, are utilized in various fields.[47,48] Among them, UiO-66 can be effectively used in biosensors due to its high biocompatibility and strong binding interactions with DNA strands.[49] In addition, amine groups ($-NH_2$) were attached to UiO-66 to facilitate its binding with various organic ligands.[50] By applying UiO-66-NH_2 to the sensing membrane, the increased contact area with biomolecules, owing to its large specific surface area, can enhance the sensor's sensitivity.[51] They also offer economic efficiency due to their potential for low-cost large-scale production.[52]

In addition to the conventional EGFET, our laboratory has developed a rapid electrochemical biosensor over the past few years.[53–56] The incorporation of alternating-current electrothermal flow (ACEF) reduced the target–bioprobe binding time, a known limitation of conventional biosensors, to less than 10 min, achieving a measurement time comparable to those of lateral flow assay (LFA)-type biosensors. The FET sensor enables quantitative analysis, which is not possible with the LFA sensor, thereby further increasing its commercialization potential.

In this study, the R-EGFET-based biosensor functionalized with HPIV aptamers and UiO-66 MOF nanoparticles was developed. The synthesized aptamers are regarded as promising alternatives to antibodies because they can be produced rapidly and at low cost.[57–59] The HPIV aptamers selected through the systematic evolution of ligands by the exponential enrichment (SELEX) process were used as bioprobes to detect HPIV in the sensors based on their high binding affinities. The specificity of the HPIV aptamer was improved, and the production cost was reduced by truncating non-target binding sequences. In addition, the introduction of ACEF technology enabled the rapid detection of HPIV. The R-EGFET biosensor successfully detected HPIV with high specificity and sensitivity in clinical samples. Fig. 1 shows a schematic diagram of the developed HPIV biosensor.

Materials and methods

Materials

The HPIV-3 HN protein (60.4 kDa) and Zika envelope protein (13 kDa) were purchased from Sino Biological (Beijing, China). Recombinant Yellow Fever Virus (YFV) NS1 protein (41 kDa) was purchased from R&D Systems (Minneapolis, USA). Bovine serum albumin (BSA), hemoglobin, myoglobin, human serum albumin, and cysteamine were purchased from Sigma-Aldrich (St Louis, MO, USA). Artificial saliva was purchased from Pickering Laboratories (California, USA). UiO-66-NH_2 was purchased from MediArk (Cheongju, South Korea). 4-(2-Hydroxyethyl)-1-piperazineethanesulfonic acid (HEPES), acetone (C_3H_5O), and anhydrous ethyl alcohol (C_2H_5OH) were purchased from Daejung (Busan, South Korea). 1-Ethyl-3-(3-dimethylaminopropyl)carbodiimide (EDC), *N*-hydroxysulfosuccinimide (Sulfo-NHS), and EZ-Link Sulfo-NHS-LC-Biotin were purchased from Thermo Fisher Scientific (MA, USA). Streptavidin magnetic beads were purchased from GenScript (New Jersey, USA). The HPIV aptamer was selected using a XELEX DNA Core Kit (EURx, Gdańsk, Poland). The DNA library sequence of the kit consists of the oligonucleotide 5′-TGA CAC CGT ACC TGC TCT-N40-AAG CAC GCC AGG GAC TAT-3′, the forward primer 5′-TGA CAC CGT ACC TGC TCT-3′, and the reverse primer 5′-ATA GTC CCT GGC GTG CTT-3′. The PCR master mix and a 100 bp DNA size marker for electrophoresis were purchased from Bioneer (Daejeon, South Korea). The HPIV aptamer was produced by Bionics with a 5′-terminal modification of the Thiol Modifier C6, and the sequence is SH-5′-CCA CAA TGG GAG TGT ATT ACG AAG CTT CAC TGG TCT GAT AAG CAC GCC AAG GGA CTA TAG AGC AGG TAC GGT GTC C-3′ (77-mer). All oligonucleotides were diluted in nuclease-free water and stored at −20 °C. We conducted a clinical experiment using cultured HPIV-1 samples. HPIV-1 (Lot No. 20210315) was provided by the Virus Bank (Seoul, South Korea). HPIV-1 was infected with LLC-MK2 cells in MEM containing 1 μg mL^{-1} TPCK-trypsin and cultured for 7 days at 37 °C and 5% CO_2. The titer of the HPIV-1 stock was 4.0×10^9 PFU per mL, which induces a cytopathic effect (CPE) in infected cells. The virus was stored at −80 °C until further use.

HPIV HN aptamer SELEX

SELEX was performed as described previously[60] to design aptamers that specifically target the HPIV HN protein. SELEX repeated eight rounds of incubation, binding, elution, and amplification. For incubation, the biotinylation step of the HPIV HN protein was carried out by mixing 50 μL of 0.25 mg mL^{-1} HPIV HN protein diluted in deionized water (DIW) with 10 μL of 2 mM Sulfo-NHS-LC-Biotin at room temperature for 1 h with stirring. The mixture was combined with 960 μL of HEPES solution and placed in a 3000 NMWL Amicon centrifugal filter (Merck, USA) to maintain a constant pH, and unreacted substances were removed through centrifugation at 7000 rpm for 30 min. The biotinylated HPIV HN protein was recovered by filtration, mixed with 100 μL of streptavidin magbeads, and they underwent a binding process by stirring for 1 h. Unbound HPIV HN protein was washed three or more times with 1× SELEX buffer. The HPIV HN protein coated with streptavidin magbeads was mixed with DNA library Bank 40 (20 μL DNA library, 20 μL 10× SELEX buffer, and 160 μL DIW) and stirred at 4 °C for 1 h to facilitate affinity binding with DNA. Nonspecifically bound DNA was removed by washing three times with 200 μL of 1× SELEX buffer. The streptavidin-coated HPIV HN protein bound to DNA was heat-treated at 80 °C for 10 min in a heat block to perform elution. After centrifugation, a magnet was used to collect the supernatant containing the dissolved DNA that selectively binds to the HPIV HN protein. For amplification of the collected DNA, 20 μL of

Published on 23 d'agost 2025. Downloaded on 7/2/2026 16:13:18.

the DNA was mixed with 2 μL of 4 μM Bank 40-5′ primer, 2 μL of 4 μM Bank 40-3′ primer, and 25 μL of 1× PCR master mix, and PCR was performed. PCR was conducted for 12 cycles under the following conditions: 4 °C for 3 min, 55 °C for 30 s, and 72 °C for 1 min. The SELEX process, consisting of four steps, was repeated for up to eight rounds; to enhance binding specificity, each round, except the first, used the DNA template amplified in the previous step. The final product from the last round was purified on a 1% agarose gel and analyzed by DNA sequencing using unidirectional RCA and vector 50 cloning at Solgent (Seoul, Korea).

Aptamer binding test for confirming selectivity

After confirming the specific binding of the HPIV HN protein to the ssDNA pool purified by SELEX through 8% Tris-borate-EDTA (TBE) polyacrylamide gel electrophoresis (PAGE), DNA sequencing analysis was performed. Duplicate or ambiguous sequences among the 50 candidate aptamers were excluded from the DNA sequencing analysis. Then, the concentration of SELEX folding buffer (140 mM Na^+ ions, 5 mM Mg^{2+} ions and 20 mM Tris (pH 7.4)) was applied to the mFold application at a room temperature of 25 °C, and the sequence with a single hybridization site and the lowest Gibbs free energy (dG) value was selected (**https://www.unafold.org**).

In the determined HPIV HN protein sequence, the unnecessary sequences used for primer recognition during PCR were removed. The removed sequence was TGA-CAC-CGT-ACC-TGC-TCT at the 5′ end. Because the number of sequences decreased, we reapplied mFold to compute the dG values. Although dG increased, the selected sequence was identified to have the lowest value among the candidates, and its secondary structure was subsequently determined.

To evaluate the performance of the truncated aptamer, a bead-based fluorescence-binding assay was performed. The binding affinity of the aptamer was determined by analyzing the fluorescence resulting from the binding interaction between the fluorescently labeled ligand and receptor (*e.g.*, protein). Fluorescein phosphoramidite (FAM), a fluorescent dye, was attached to the 5′ end of the aptamer, and the fluorescence intensity was measured at concentrations of 10 nM, 30 nM, 150 nM, 300 nM, 750 nM, and 1 μM. The maximum absorbance was set at 1.2 μM. Fluorescence was measured based on the degree of binding between the aptamer and magnetic beads conjugated with the HPIV HN protein at an absorbance of 480 nM and emission of 528 nM using a BioTek Synergy LX Multimode Reader (Vermont, USA). The K_d value of the aptamer was confirmed, and the HPIV aptamer was selected as the probe for the sensor.

Fabrication of the HPIV biosensing platform

The Au microgap electrode was prepared as previously described.[61] UiO-66-NH_2 at 1 mg mL^{-1} was diluted in DIW and sonicated for 10 min to obtain a homogeneous suspension before use. The electrode was sonicated in acetone for 10 min, washed sequentially with ethanol and distilled water, and dried with N_2 gas. 2 μL of 10 mM cysteamine was immobilized on the washed Au electrode for 1 h to form an NH_2 layer. EDC (20 mM) and NHS (50 mM) were reacted with UiO-66-NH_2 at room temperature for 15 min to activate the NHS-ester, followed by immobilization on the electrode for 3 h. The electrode functionalized with UiO-66-NH_2 was treated with a 1 μM 5′-SH-modified HPIV aptamer and reacted for 3 h. Subsequently, the electrode was washed with DIW and dried with N_2 gas.

Ethical approval and patient enrollment

This study was conducted under approval from the Yeungnam University Institutional Review Board (IRB No. YUMC 2021-02-053-001). Patients presenting with acute respiratory symptoms (*e.g.*, pneumonia and bronchiolitis) and suspected HPIV infection were enrolled. Exclusion criteria included recent antiviral therapy (<7 days) or insufficient bronchoalveolar lavage fluid (BALF) volume for analysis.

BALF collection

BALF was obtained *via* standardized bronchoscopy under sterile conditions. The bronchoscope was wedged into the affected bronchus, and three sequential aliquots (20 mL each) of sterile saline were instilled and aspirated. The first aliquot, enriched with epithelial cells, was prioritized for viral testing. BALF was centrifuged at 400*g* for 10 min to obtain pellet cellular debris. Supernatants were aliquoted into cryovials and stored at −80 °C until analysis.

Characterization of UiO-66

The morphology and particle size of UiO-66-NH_2 were examined using field-emission scanning electron microscopy (FE-SEM). Surface analysis was performed by investigating the morphology, roughness, and vertical distance of the UiO-66 layer formed on the Au electrode using atomic force microscopy (AFM) (XE7; Park Systems, South Korea). In the AFM measurements, the cantilever was set at a resonance frequency of 330 kHz and a spring constant of 42 N m^{-1}, and screening was performed using a PPP-NCHR silicon tip (Park Systems, Korea). Optimization settings, such as scan speed and amplitude, were based on a previous study.[62]

Electrical characterization using the EGFET and ACEF technique

Electrical characteristics, such as the relationship between the drain current (I_D) and gate voltage (V_G), were analyzed using a source meter (Keithley 2614b; Keithley, Cleveland). The EGFET device used in this study consisted of an Au electrode connected to the gate terminal of a commercial n-type metal–oxide–semiconductor FET (MOSFET) device (CD4007; Texas Instruments, Texas) and an Ag/AgCl reference electrode (CHI111; Qrins, Seoul, South Korea). The Au electrode was used as the sensing membrane, and the extended gate facilitated biomolecule immobilization by isolating the FET from the chemical environment.[63] The Ag/AgCl reference electrode was immersed in a chamber containing 1× PBS buffer (pH

 This journal is © The Royal Society of Chemistry 2025

Published on 23 d'agost 2025. Downloaded on 7/2/2026 16:13:18.

7.5), and a voltage was applied to the gate. 1× PBS has a low viscosity and can minimize Debye screening, making it useful for maintaining consistent signal values during measurements.[64] The V_G applied to the reference electrode was swept from 0 to 2 V, and I_D was measured with the drain voltage (V_D) fixed at 0.05 V while the source terminal was electrically grounded. By maintaining a constant drain voltage, the linearity of the drain current is ensured, enhancing the stability and accuracy of the signal.[65] The threshold voltage (V_t) is defined as the gate voltage at which the current flows in the range of 1 μA to 1 nA. All the measurements were conducted at room temperature and repeated 12 times (n = 12) to ensure reproducibility and reliability. ACEF was performed using a function generator (Tektronix, Beaverton, OR, USA). An alternating current (AC) signal with an amplitude of 3 V and frequency of 1 MHz was applied to the working electrode (WE) and counter electrode (CE).[66] After the binding of the target substance *via* ACEF, washing with DIW was performed to remove excessively adsorbed non-specific molecules.

Statistical analysis

SPSS software (version 20.0; IBM Corp., Armonk, NY, USA) was used to calculate the standard and equilibrium electrical measurement errors of the data. Box plots were analyzed using Origin software v.2019 (OriginLab, USA). One-way analysis of variance (ANOVA) was conducted to statistically analyze the significant differences and selectivity between the data groups, followed by *post-hoc* tests using Tukey's HSD and LSD algorithms. The probability (p) values are expressed as follows: $*p < 0.05$, $**p < 0.01$, and $***p < 0.005$. In addition, the diagnostic accuracy and false-positive rate of the sensor were analyzed using a receiver operating characteristic (ROC) curve. The optimal cut-off value for disease diagnosis was determined based on the Youden index, which is defined as "sensitivity + specificity − 1".[67] Sensor performance was evaluated using indices such as the area under the curve (AUC), specificity, and sensitivity at specific thresholds.[68,69]

Results and discussion

HPIV aptamer performance analysis

The selectivity of the HPIV aptamer for its target protein using 8% native TBE-PAGE is shown in Fig. 2a. Except for lanes 1 and 2, band changes were observed according to the binding of the aptamer. Hemoglobin, BSA, and YFV NS1 proteins were used as controls for HPIV HN protein. The band shape changed because of complement binding to the HPIV HN protein, whereas the bands of the other proteins showed only minimal changes. Therefore, we demonstrated that the fabricated HPIV aptamer specifically binds to its target protein, HPIV HN. The HPIV aptamer was modified at the 5′ end with a Thiol Modifier C6 to facilitate its application to the sensor.

The 2D and 3D structures of the truncated HPIV aptamer are shown in Fig. 2b. The 2D structure was predicted using mFold at 25 °C with a buffer composed of 140 mM Na^+ and 5 mM Mg^{2+} ions. The 3D structure of the HPIV aptamer was obtained using the 3dRNA/DNA web server (**https://biophy.hust.edu.cn/new/3dRNA/create**) based on the dot-bracket notation (Vienna format) of its 2D structure. The 3D structure of the HPIV aptamer was downloaded from the Protein Data Bank (PDB) format and applied to a visualization viewer, allowing for a detailed examination of the structure *via* RCDBPDB (**https://www.rcsb.org/3d-view**). The binding affinity of the HPIV aptamer is shown in Fig. 2c. A FAM group was introduced at the 5′ end of the aptamer, and its dissociation constant was determined using bead-based fluorescence analysis. Based on the fluorescence intensity at different aptamer concentrations, the binding affinity (K_d) of the aptamer was calculated using the adsorption eqn (1).

$$\theta = (\gamma - \gamma_F)/(\gamma_R - \gamma_F) = (1/2[\text{DNA aptamer}])(K_d + x + [\text{DNA aptamer}])(K_d + x + [\text{DNA aptamer}]^2 - 4[\text{DNA aptamer}]x)^{1/2} \quad (1)$$

where θ is the percentage of bound protein, x is the protein concentration, and γ is the fluorescence intensity observed in

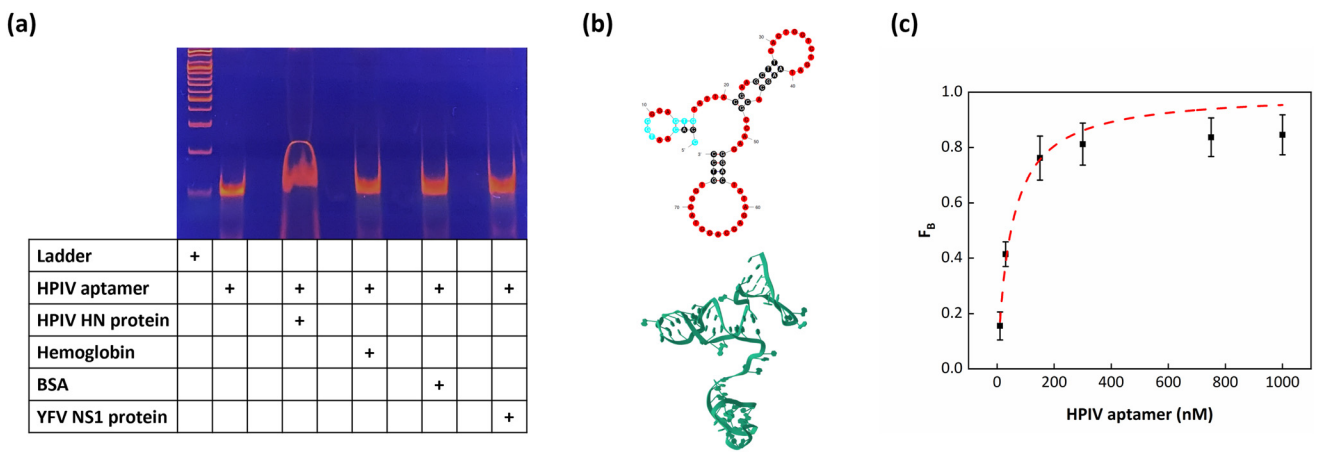

Fig. 2 (a) The 8% TBE-PAGE results of the HPIV aptamer. (b) Structure of the truncated HPIV aptamer: the upper image shows the 2D structure and the lower image shows the 3D structure. (c) Binding affinity of the truncated HPIV aptamer (K_d = 48.483 ± 7.555 nM).

Published on 23 d'agost 2025. Downloaded on 7/2/2026 16:13:18.

the nth titration. γ_F is the fluorescence intensity in the absence of protein, and γ_R is the fluorescence intensity at the saturation protein concentration. Finally, the K_d value of the HPIV aptamer was calculated to be 48.483 ± 7.555 nM.

Surface morphology investigation of the UiO-66 MOF layer

The morphology and particle size of UiO-66-NH_2 were examined using FESEM. Fig. S1a shows that UiO-66-NH_2 was widely spread on Au to form a layer. UiO-66-NH_2 was observed as relatively uniform octahedral crystals with a particle size of approximately 250 nm (Fig. S1b).

Surface analysis of the Au electrode at each immobilization step was performed using AFM in non-contact mode to minimize damage to the biological samples. Surface parameters such as the vertical distance (VD), average roughness (R_a), and root mean square roughness (R_q) were analyzed to confirm the immobilization of the materials. Fig. 3a shows the surface of the non-uniform Au electrode, confirming the absence of any material other than Au. The bare electrode exhibited a VD of 2.442 ± 0.431 nm, R_a of 0.628 ± 0.101 nm, and R_q of 0.717 ± 0.114 nm, indicating a smooth surface. Fig. 3b shows an image of UiO-66-NH_2 immobilized on the Au electrode. UiO-66-NH_2 expanded the binding area of the HPIV aptamer due to its large specific surface area. UiO-66-NH_2 exhibited its characteristic geometric structure in a spread-out form, and the increase in surface VD to approximately 17.756 ± 1.389 nm indicates successful immobilization. The R_a and R_q values also increased to 6.212 ± 1.962 nm and 7.154 ± 1.730 nm, respectively, compared with those of the bare electrode. When the aptamer and UiO-66-NH_2 were combined, the VD was 41.378 ± 0.683 nm, R_a was 15.484 ± 0.604 nm, and R_q was 17.136 ± 1.262 nm (Fig. 3c). Considering that the size of 1-mer is approximately 0.34 nm, the maximum theoretical length of the 77-mer aptamer is estimated to be 26.18 nm. The error of about 2–3 nm is thought to be due to the non-uniform height of the UiO-66-NH_2 particles and the three-dimensional folding of the aptamer. Fig. 3d shows the image after the aptamer and HPIV HN protein were combined. The spherical HPIV HN protein bound to the UiO-66-NH_2/aptamer to form a complex, with VD = 61.777 ± 1.022 nm, R_a = 22.410 ± 0.363 nm, and R_q = 25.407 ± 0.182 nm. All values were calculated by averaging measurements from three regions where the particles were present. The AFM results demonstrated that UiO-66-NH_2, the aptamer, and the HPIV HN protein were successfully immobilized on the Au electrode (Table 1).

Table 1 Surface analysis of Au, UiO-66-NH_2, UiO-66-NH_2/aptamer, and UiO-66-NH_2/aptamer/HPIV HN protein

Measuring substance	Vertical distance (VD) (nm)	RMS roughness (R_q) (nm)	Roughness average (R_a) (nm)
Bare	2.442 ± 0.431	0.717 ± 0.114	0.628 ± 0.101
UiO-66-NH_2	17.756 ± 1.389	7.154 ± 1.730	6.212 ± 1.962
UiO-66-NH_2/aptamer	41.378 ± 0.683	17.136 ± 1.262	15.484 ± 0.604
UiO-66-NH_2/aptamer/HPIV HN protein	61.777 ± 1.022	25.407 ± 0.182	22.410 ± 0.363

Surface characterization of functionalized electrodes

Electrical biosensing detects changes influenced by the intrinsic charge of biomolecules. When biomolecules such as nucleic acids or proteins are immobilized on the sensing electrode, a change in the dielectric layer occurs at the interface between the channel and electrolyte. Changes in the dielectric layer affect the electrical potential of the channel, leading to variations in the drain current, which are reflected in the sensor's output signal.[70] The sensing capability of an EGFET can be evaluated through the I_D–V_G curve. This curve exhibits a positive correlation with V_t, a key variable that indicates the sensitivity of the EGFET. The electrical characteristic changes at each functionalization stage of the electrode for HPIV detection can be confirmed through the I_D–V_G curve and V_t value (Fig. 4a and b). The detection of the EGFET sensor is confined within the electrolyte solution due to the screening effect of the ionic liquid and is sensitive to the Debye length (λ_D), which varies with ionic strength.[71,72] Therefore, to increase protein detection sensitivity in a physiological environment, an appropriate electrolyte solution that can overcome λ_D is required.[73] In this study, we used 1× PBS to electrically characterize the extended gate within λ_D. 1× PBS can prevent the reduction in protein activity and binding affinity caused by protein denaturation.[74] Considering that the λ_D of 1× PBS is approximately 0.74 nm, UiO-66 could induce electrical properties on the extended gate surface by remaining close to the

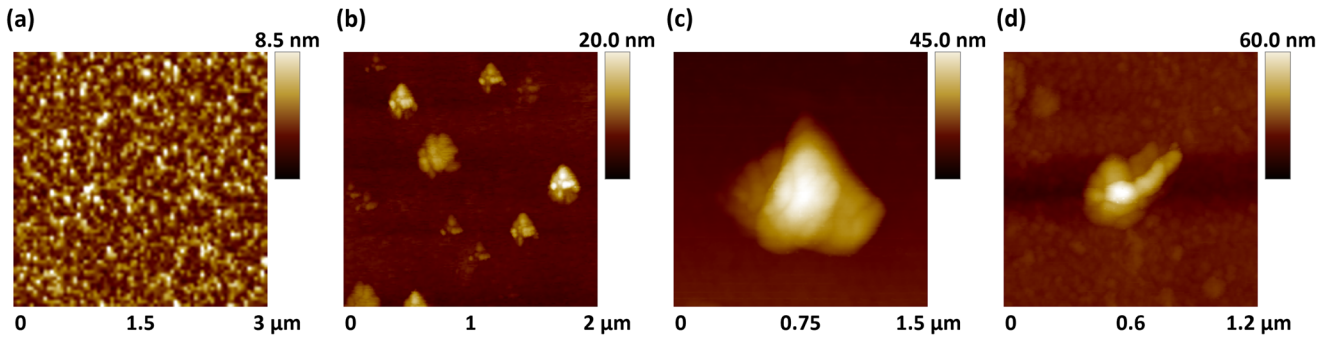

Fig. 3 AFM images of (a) bare, (b) UiO-66-NH_2, (c) UiO-66-NH_2/aptamer, and (d) UiO-66-NH_2/aptamer/HPIV HN protein.

 This journal is © The Royal Society of Chemistry 2025

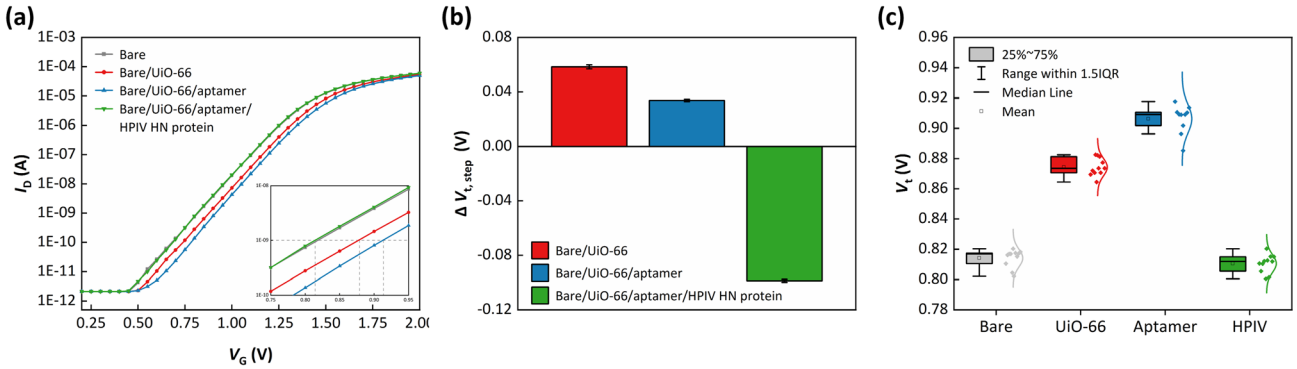

Fig. 4 (a) I_D–V_G curves from the immobilization step. (b) ΔV_t values from the immobilization step. (c) Box plot showing the reproducibility of the ΔV_t value according to the immobilization step. Boxplots indicate the IQR from 25 to 75% per condition, and whiskers represent ± 1.5 IQR.

Published on 23 d'agost 2025. Downloaded on 7/2/2026 16:13:18.

conductive surface as long as the 0.702 nm length of the cysteamine linker is within the λ_D range. Accordingly, the electrical characterization of each electrode functionalization step was verified through the behavior of V_t in response to changes in the charge at the electrode interface. An n-type FET uses electrons as the primary carriers. The electric field between the gate and the channel depends on the surface charge of the sensing membrane, affecting the channel current and V_t.[75] As the negative charge density on the membrane increased, the negative charge suppressed the electron carriers, leading to an increase in V_t. The amine groups of UiO-66-NH_2 are negatively charged in the neutral DIW environment. UiO-66-NH_2 accumulated negative charges on the membrane surface, leading to an increase in V_t and a positive shift in the I_D–V_G curve (Fig. 4a). Subsequently, when the aptamer was immobilized, a negative charge was induced in the membrane owing to the negative charge of DNA, and V_t increased compared with the previous step. The electrical properties of proteins, which are amphoteric molecules, are predominantly influenced by the pH of the solvent based on the isoelectric point (pI).[76] The pI of HPIV HN protein is approximately 7.37. The positively charged HPIV HN protein in DIW (pH 7) bound to the aptamer, which neutralized the negative charge on the membrane, resulting in a decrease in V_t. Fig. 4b shows $\Delta V_{t,\ step}$; $\Delta V_{t,\ step}$ is calculated using eqn (2) as follows:

$$\Delta V_{t,step} = (V_t \text{ of current electrode conditions}) - (V_t \text{ of previous electrode conditions}) \quad (2)$$

The reproducibility of the fabricated R-EGFET biosensor is presented using a box plot and a normal distribution (Fig. 4c). The box plot was visualized using the V_t values. The data in the graph are expressed in the interquartile range (25–75%), and all data (n = 10) showed a normal distribution.

Biosensor performance evaluation

To evaluate the HPIV detection performance of the fabricated biosensor, V_t values were measured for various concentrations of HPIV HN protein diluted in DIW and 10% human serum. All experimental results were measured at least 10 times per sample, and the average values were calculated. As the concentration of HPIV HN protein increased, biocomplexes were formed, and the I_D–V_G curve shifted parallel to the negative direction (Fig. 5a). A calibration curve was plotted using the ΔV_t values to determine the sensitivity of the sensor (Fig. 5b). ΔV_t was calculated using eqn (3):

$$\Delta V_t = (V_{t,blank} - V_{t,target})/V_{t,blank} \quad (3)$$

where $V_{t,\ target}$ is the V_t when the sensing platform reacts with HPIV HN protein at each concentration and $V_{t,\ blank}$ is the V_t of the blank sample. ΔV_t values were linearly proportional to $\log_{10}$[HPIV HN protein] and were 0.0280 ± 2.7 × 10^3, 0.0459 ± 9.1 × 10^4, 0.0613 ± 3.4 × 10^4, 0.0781 ± 3.1 × 10^4, 0.0947 ± 5.0 × 10^4, and 0.1124 ± 5.8 × 10^4 V for the concentration range of 1 pM to 100 nM. The calibration curve equation had a slope of 0.017 and a y-intercept of 0.028, demonstrating high linearity with an R^2 value of 0.9994. The limit of detection (LOD) was calculated based on 3.3 (standard deviation/slope) and was 22.254 fM. This indicated that the HPIV EGFET sensor was highly sensitive and specific to the HPIV HN protein.

The sensitivity of the sensor can be affected by the interference caused by non-specific binding with non-target proteins or other biomolecules in the serum.[77] We investigated the clinical applicability of the fabricated sensor using HPIV HN protein diluted in 10% human serum. The I_D–V_G curve shifted to the left owing to the formation of biocomplexes as the HPIV HN protein concentration increased, and the degree of the shift was proportional to the concentration (Fig. 5c). ΔV_t values were 0.0308 ± 1.5 × 10^3, 0.0546 ± 9.1 × 10^4, 0.0758 ± 5.3 × 10^4, 0.0978 ± 4.8 × 10^4, 0.1202 ± 9.6 × 10^4, and 0.1420 ± 3.2 × 10^4 V for the concentration range of 1 pM to 100 nM (Fig. 5d). The sensor response yielded a linear calibration curve (slope = 0.022, y-intercept = 0.032, R^2 = 0.9999), with a limit of detection calculated to be 36.202 fM. All values were calculated using the same method used for the DIW.

Selectivity is a key factor in evaluating the diagnostic performance. The selectivity of a sensor is its ability to accurately recognize only the specific target substance to be detected and minimize non-specific reactions to non-target substances.

Published on 23 d'agost 2025. Downloaded on 7/2/2026 16:13:18.

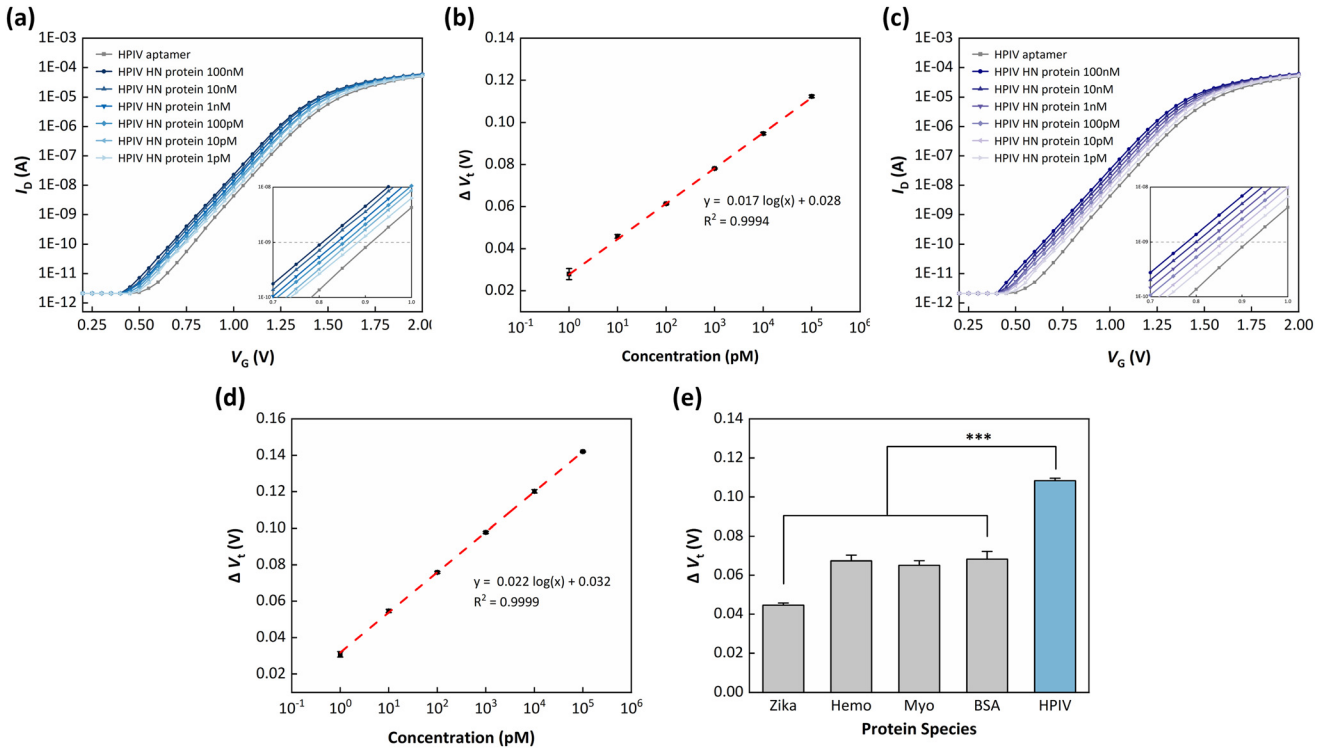

Fig. 5 (a) I_D–V_G curves by HPIV HN protein concentration (diluted in DIW). (b) Calibration curve of ΔV_t values according to HPIV HN protein concentration (diluted in DIW). (c) I_D–V_G curves by HPIV HN protein concentration (diluted in 10% human serum). (d) Calibration curve of ΔV_t values according to HPIV HN protein concentration (diluted in 10% human serum). (e) Selectivity test: comparison of significant differences between HPIV and non-target species ($p < 0.005$).

Selectivity testing is essential not only for verifying sensor performance but also for determining whether it can provide valid and reliable results in real-field diagnostics.[78] Fig. 5e shows the results of a selectivity experiment comparing the binding of Zika, hemoglobin, myoglobin, and BSA at a concentration of 1 μM. ΔV_t values were measured in the same manner as for HPIV. The four types of nontarget proteins induced positive charges on the sensing membrane, leading to a decrease in V_t, similar to the results observed with HPIV. However, the non-target proteins exhibited lower ΔV_t values compared with the target protein, indicating a significant difference from HPIV ($p < 0.005$). This indicates that the HPIV aptamer selectively recognizes and binds to HPIV, thereby preventing interference from other proteins. Consequently, we demonstrated that the HPIV aptamer-based biosensor could specifically detect HPIV.

Detection of HPIV-1 in clinical samples

Human saliva contains various biomarkers that can be used for disease diagnosis and monitoring.[79] In addition, saliva is an attractive diagnostic tool as it can be collected non-invasively, offering greater convenience and safety than blood.[80] Artificial saliva has specific ion concentrations and pH conditions similar to those of human saliva. To evaluate the clinical performance of the prepared biosensor, HPIV-1 was spiked into 3% artificial saliva at concentrations ranging from 1.0×10^1 to 1.0×10^4 PFU per mL. The prepared samples were immobilized on the sensing membrane, and the I_D–V_G signal was measured in the same manner as for HPIV HN protein. The I_D–V_G curve shifted in the negative direction upon HPIV-1 detection by the HPIV aptamer (Fig. 6a). ΔV_t values were linearly proportional to $\log_{10}$[HPIV-1] and were 0.1261 ± 0.0047, 0.1451 ± 0.0031, 0.1921 ± 0.0025, and 0.2145 ± 0.0025 V for the concentration range of 1.0×10^1 to 1.0×10^4 PFU per mL (Fig. 6b). The sensor response yielded a calibration curve (slope = 0.032, y-intercept = 0.090, R^2 = 0.9470), with a limit of detection calculated to be 9.961 PFU per mL. The relatively lower R^2 value compared with that of the HPIV HN protein can be explained by the interference caused by the nonspecific binding of non-target biomolecules in artificial saliva. Nevertheless, the low detection limit demonstrated the sensor's high selectivity and sensitivity for HPIV-1 under clinically relevant conditions.

As part of investigating the field applicability of the proposed biosensing platform, experiments were conducted using 20 positive samples (PS) and 20 negative samples (NS). PS contained randomly diluted HPIV-1 within the linear range in 3% artificial saliva, while NS consisted of blank 3% artificial saliva. The $|\Delta V_{t,\ step}|$ values of HPIV-1 PS and NS are presented in Fig. 6c. An independent two-sample t-test revealed a statistically significant difference between the two groups ($p < 0.0001$). However, the overlapping $|\Delta V_{t,\ step}|$ values between PS and NS may result in false positives and false negatives.

 This journal is © The Royal Society of Chemistry 2025

Published on 23 d'agost 2025. Downloaded on 7/2/2026 16:13:18.

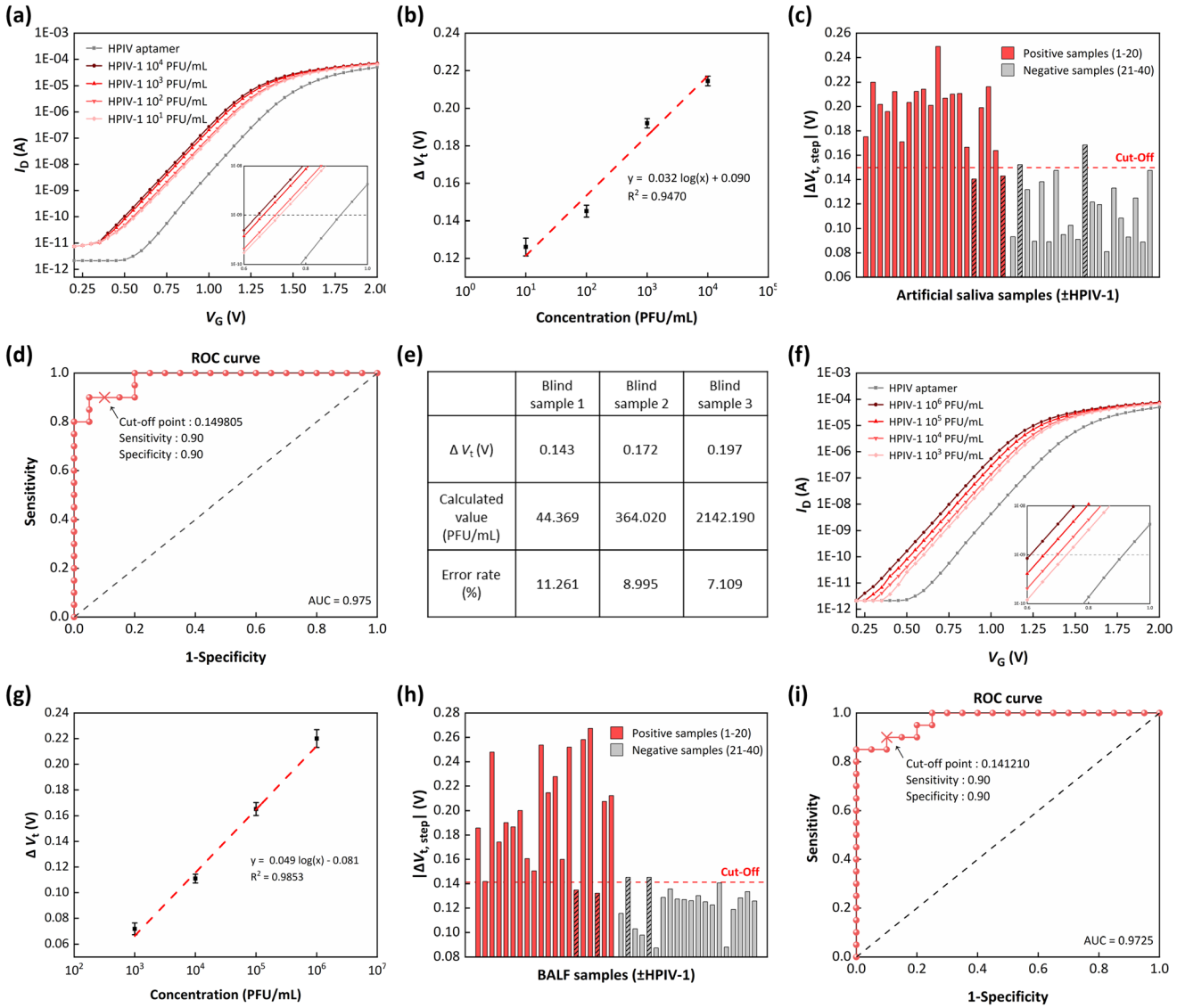

	Blind sample 1	Blind sample 2	Blind sample 3
Δ V_t (V)	0.143	0.172	0.197
Calculated value (PFU/mL)	44.369	364.020	2142.190
Error rate (%)	11.261	8.995	7.109

Fig. 6 (a) I_D–V_G curves with HPIV-1 concentration (diluted in 3% artificial saliva). (b) Calibration curves of ΔV_t values according to the HPIV-1 concentration (diluted in 3% artificial saliva). (c) False-positive test: $|\Delta V_{t,\ step}|$ values of the sensor targeting HPIV-1 in 3% artificial saliva. Red dashed line indicates the cut-off. (d) ROC curve for HPIV-1 detection in 3% artificial saliva (AUC: 0.975, asymptotic 95% confidence interval: 0.937–1.000). (e) Blind test results of the biosensor. (f) I_D–V_G curves with HPIV-1 concentration (diluted in 5% BALF). (g) Calibration curve using ΔV_t values according to the HPIV-1 concentration (diluted in 5% BALF). (h) False-positive test: $|\Delta V_{t,\ step}|$ values of the sensor targeting HPIV-1 in 5% BALF. Red dashed line indicates the cut-off. (i) ROC curve for HPIV-1 detection in 5% BALF (AUC: 0.9725, asymptotic 95% confidence interval: 0.932–1.000).

Therefore, the monitoring performance of the sensor was evaluated more accurately using the ROC curve (Fig. 6d). The ROC curve is a plot that can effectively measure the diagnostic performance through the trade-off between sensitivity and 1-specificity. The AUC represents the area under the ROC curve. The closer the AUC is to 1, the higher the accuracy of the sensor. The AUC was 0.975, and the optimal threshold voltage (cut-off) was defined as 0.149805 V (Fig. 6d). The biosensor demonstrated 90% sensitivity and 90% specificity, correctly classifying 18 PS and 18 NS (Fig. 6c).

To verify the detection accuracy of the sensor, different concentrations of HPIV-1 diluted in 3% artificial saliva were used in a blind test (Fig. 6e). Samples with concentrations of 5.0×10^1, 4.0×10^2, and 2.0×10^3 PFU per mL were prepared for the experiment. After measuring the I_D–V_G signal using the EGFET, the obtained V_t values were substituted into the calibration curve, resulting in concentrations of 44.369, 364.020, and 2142.190 PFU per mL. The calculated sample concentrations showed low error rates of 11.261, 8.995, and 7.109%, respectively. These results confirm the biosensor's quantitative performance and detection reliability.

To further evaluate the clinical applicability of the biosensor, we conducted additional experiments using BALF, a diagnostically relevant specimen obtained from the lower respiratory tract. BALF provides enhanced diagnostic accuracy for respiratory pathogens due to its direct origin from the alveolar

Table 2 Comparison of HPIV detection systems reported in the literature

Method	Target	Detection time	Detection range	LOD	Ref.
Multiplex reverse transcription PCR	RSV PIV ADV	1–2 h	2.0×10^{-1}–2.5×10^{2} $TCID_{50}$ per mL	2.0×10^{-1} $TCID_{50}$ per mL	82
Multiplex reverse transcription PCR	HPIV-1 HPIV-2 HPIV-3 HPIV-4	2 h	4.0×10^{-4}–3.2×10^{1} $TCID_{50}$ per mL	4.0×10^{-4} $TCID_{50}$ per mL	83
Real time qPCR	HPIV-1	—	1.0×10^{0}–1.0×10^{8} copies per reaction	1 copy per reaction	84
Multiplex reverse transcription PCR	HPIV-1 HPIV-3	—	1.0×10^{0}–1.0×10^{6} copies per reaction	1 copy per reaction; 1.0×10^{-2} $TCID_{50}$ per mL	85
Electrical – EGFET	HPIV-1	10 min	1.0×10^{1}–1.0×10^{4} PFU per mL	1.382 PFU per mL	In this study

Published on 23 d'agost 2025. Downloaded on 7/2/2026 16:13:18.

and bronchiolar regions.[81] HPIV-1 was spiked into 5% BALF at concentrations ranging from 1.0×10^{3} to 1.0×10^{6} PFU per mL. The resulting I_D–V_G curves exhibited concentration-dependent shifts comparable to those observed in artificial saliva (Fig. 6f). ΔV_t values for the concentration range (1.0×10^{3} to 1.0×10^{6} PFU per mL) were 0.0718 ± 0.0046, 0.1110 ± 0.0034, 0.1653 ± 0.0051 and 0.2201 ± 0.0069 V (Fig. 6g). The sensor response yielded a linear calibration curve (slope = 0.049, y-intercept = −0.081, R^2 = 0.9853), with a limit of detection calculated to be 15.273 PFU per mL. The storage stability and reproducibility of the proposed sensing platform were evaluated over various storage periods (Fig. S2). The electrodes functionalized with UiO-66-NH_2 and HPIV aptamers were stored in a dry state at room temperature, and the signal values were measured by applying HPIV-1 using ACEF daily at the same time. The ΔV_t values remained within the established 95% confidence interval compared to the initial (Day 0) measurement for up to three days. However, the signal began to deviate from the confidence interval on Day 4, and by Day 7, it had decreased by approximately 51.33% relative to the initial value. This suggests that the prepared biosensor can reliably detect HPIV-1 for up to three days. The field applicability of the sensor was also evaluated using BALF samples. A total of 40 samples were tested, comprising 20 PS containing randomly diluted HPIV-1 within the linear range and 20 NS consisting of blank 5% BALF. The significant difference between the two groups in Fig. 6h was confirmed by an independent two-sample t-test ($p < 0.0001$). Based on the ROC analysis, the AUC was 0.9725, and the cut-off voltage was 0.141210 V (Fig. 6i). The biosensor demonstrated 90% sensitivity and 90% specificity, correctly classifying 18 PS and 18 NS. These results underscore the sensor's robustness and potential for clinical translation in complex respiratory matrices.

According to the literature, RT-PCR is the primary method used to detect HPIV infection. However, multiplex reverse transcription PCR (Table 2) exhibited a long detection time and a high detection limit for HPIV. Compared with previously investigated methods, the biosensor developed in this study enables sensitive detection with minimal binding time. This can be attributed to the successful introduction of ACEF into the EGFET and the application of a specifically designed aptamer. Ultimately, we engineered an R-EGFET-based biosensor for HPIV detection, which, with its high sensitivity and specificity, has the potential for on-site detection of HPIV.

Conclusions

Through the COVID-19 pandemic, the importance of diagnosing and preventing respiratory viruses that periodically pose significant threats to humanity has been highlighted more than ever. Until now, field diagnostics have predominantly relied on LFA-based strip sensors. However, LFA sensors are limited in that they cannot perform quantitative analysis, and their accuracy decreases when the signal is weak. In contrast, FET-based biosensors offer high sensitivity and enable quantitative analysis, but their long target-bioprobe binding time has posed challenges for commercialization. The proposed ACEF-based R-EGFET biosensor represents an effort to overcome these challenges and drastically enhance analysis speed. The truncated aptamer significantly reduced production costs while maintaining sensitivity comparable to that of antibodies. Electrical biosensing platforms enable real-time monitoring with high sensitivity, low cost, and rapid diagnosis. UiO-66 MOF nanoparticles were introduced to provide a large surface area to the sensor and improve its electrical sensitivity. By applying the ACEF technology, the target detection time was effectively shortened, enabling rapid diagnosis. The newly designed HPIV aptamer exhibited outstanding detection capability, with detection limits of 22.254 and 36.202 fM in buffer and human serum, respectively. The biosensor successfully detected HPIV-1 in clinical samples, demonstrating its potential for clinical application. The limits of detection were 9.961 PFU per mL and 15.273 PFU per mL in artificial saliva and BALF, respectively, with the corresponding AUC values of 0.975 and 0.9725. ROC analysis confirmed the diagnostic sensitivity and specificity to be 90% for both sample types, validating the biosensor's accuracy and reliability. In conclusion, the fabricated biosensor was demonstrated to be an innovative platform that can be utilized for HPIV clinical diagnosis based on its rapid and sensitive detection performance.

 This journal is © The Royal Society of Chemistry 2025

Author contributions

Siyun Lee: investigation, experimentation, visualization, data curation and writing – original draft. Nayeon Kwon: investigation, data curation and writing – review & editing. Yejin Yoon: data curation and validation. Jinho Yoon: data curation and validation. Jong Geol Jang: data curation and validation. Wonhwa Lee: writing – review & editing and supervision. Jin-Ho Lee: supervision. Chulhwan Park: supervision. Taek Lee: conceptualization, writing – review & editing, and supervision.

Conflicts of interest

There are no conflicts to declare.

Data availability

The data supporting this article have been included as part of the SI. The Supplementary Information provides additional characterization data and stability evaluation of the fabricated biosensor. See DOI: **https://doi.org/10.1039/d5nr01979f**.

Acknowledgements

This work was supported by the National Research Foundation of Korea (NRF) grant funded by the Korea Government (MSIT) (No. 2021R1C1C1005583, RS-2024-00416117, and 2022R1A5A2027161).

Published on 23 d'agost 2025. Downloaded on 7/2/2026 16:13:18.

References

1 W. Liu, Q. Liu, D. Chen, H. Liang, X. Chen, W. Huang, S. Qin, Z. Yang and R. Zhou, *BMC Infect. Dis.*, 2013, **13**, 1–8.
2 N. Xiao, Z. Duan, Z. Xie, L. Zhong, S. Zeng, H. Huang, H. Gao and B. Zhang, *J. Med. Virol.*, 2016, **88**, 2085–2091.
3 S. Essa, H. Al-Tawalah, S. AlShamali and W. Al-Nakib, *Virol. J.*, 2017, **14**, 1–7.
4 S. Zhou, N. Mao, Y. Zhang, A. Cui, Z. Zhu, R. Hu, J. Xu and W. Xu, *Arch. Virol.*, 2021, **166**, 2585–2590.
5 Z. Zhu, Y. Zhang and N. Mao, *World J. Pediatr.*, 2025, 1–3.
6 A. Steffens, L. Finelli, B. Whitaker and A. Fowlkes, *Pediatr. Infect. Dis. J.*, 2016, **35**, 717–722.
7 F. Scaggs Huang, D. I. Bernstein, K. S. Slobod, A. Portner, T. Takimoto, C. J. Russell, M. Meagher, B. G. Jones, R. E. Sealy and C. Coleclough, *Hum. Vaccines Immunother.*, 2021, **17**, 554–559.
8 N. P. DeGroote, A. K. Haynes, C. Taylor, M. E. Killerby, R. M. Dahl, D. Mustaquim, S. I. Gerber and J. T. Watson, *J. Clin. Virol.*, 2020, **124**, 104261.
9 R. Pecchini, E. N. Berezin, M. C. Souza, L. d. A. Vaz-de-Lima, N. Sato, M. Salgado, M. Ueda, S. D. Passos, R. Rangel and A. Catebelota, *Braz J Infect Dis.*, 2015, **19**, 358–362.
10 M. A. Swamy, B. Malhotra, P. J. Reddy, N. Kumar, J. K. Tiwari and M. L. Gupta, *Indian J. Pediatr.*, 2016, **83**, 1109–1113.
11 S. J. Olsen, A. K. Winn, A. P. Budd, M. M. Prill, J. Steel, C. M. Midgley, K. Kniss, E. Burns, T. Rowe and A. Foust, *Am. J. Transplant.*, 2021, **21**, 3481–3486.
12 L. Wang, S. Lu, Y. Guo, J. Liu, P. Wu and S. Yang, *Virol. J.*, 2023, **20**, 245.
13 Y. Pan, Y. Zhang, W. Shi, X. Peng, S. Cui, D. Zhang, G. Lu, Y. Liu, S. Wu and P. Yang, *Influenza Other Respir. Viruses*, 2017, **11**, 564–568.
14 Y. Lin, M. Khan, B. Weynand, M. Laporte, F. Coenjaerts, D. Babusis, J. P. Bilello, P. Mombaerts, D. Jochmans and J. Neyts, *Nat. Commun.*, 2024, **15**, 7765.
15 B. S. Pritt and M. C. Aubry, *Seminars in Diagnostic Pathology*, 2017, **34**, 510–517.
16 G. M. Loughlin and A. Moscona, *Pediatr. Clin. North Am.*, 2006, **53**, 929.
17 A. Azevedo, E. L. Durigon, V. Okasima, D. Queiroz, D. de Moraes-Vasconcelos, A. J. d. S. Duarte and A. S. Grumach, *Allergol. Immunopathol.*, 2003, **31**, 311–317.
18 M. Pawełczyk and M. L. Kowalski, *Curr. Allergy Asthma Rep.*, 2017, **17**, 1–10.
19 A. C. Schmidt, A. Schaap-Nutt, E. J. Bartlett, H. Schomacker, J. Boonyaratanakornkit, R. A. Karron and P. L. Collins, *Expert Rev. Respir. Med.*, 2011, **5**, 515–526.
20 X. Zhan, K. S. Slobod, S. Krishnamurthy, L. E. Luque, T. Takimoto, B. Jones, S. Surman, C. J. Russell, A. Portner and J. L. Hurwitz, *Vaccine*, 2008, **26**, 3480–3488.
21 M. C. Lawrence, N. A. Borg, V. A. Streltsov, P. A. Pilling, V. C. Epa, J. N. Varghese, J. L. McKimm-Breschkin and P. M. Colman, *J. Mol. Biol.*, 2004, **335**, 1343–1357.
22 M. Porotto, M. Fornabaio, O. Greengard, M. T. Murrell, G. E. Kellogg and A. Moscona, *J. Virol.*, 2006, **80**, 1204–1213.
23 K. J. Henrickson, *Clin. Microbiol. Rev.*, 2003, **16**, 242–264.
24 M. Welch, K. Krueger, J. Zhang, P. Piñeyro, R. Magtoto, C. Wang, L. Giménez-Lirola, E. Strait, M. Mogler and P. Gauger, *BMC Vet. Res.*, 2022, **18**, 110.
25 A. R. Branche and A. R. Falsey, *Seminars in Respiratory and Critical Care Medicine*, 2016, **37**, 538–554.
26 M. E. Terlizzi, B. Massimiliano, S. Francesca, F. Sinesi, V. Rosangela, G. Stefano, C. Costa and C. Rossana, *J. Virol. Methods*, 2009, **160**, 172–177.
27 G. Seo, G. Lee, M. J. Kim, S. Baek, M. Choi, K. B. Ku, C. Lee, S. Jun, D. Park and H. G. Kim, *ACS Nano*, 2020, **14**, 5135–5142.
28 B. Wang, C. Zhao, Z. Wang, K. Yang, X. Cheng, W. Liu, W. Yu, S. Lin, Y. Zhao and K. M. Cheung, *Sci. Adv.*, 2022, **8**, eabk0967.
29 J. Wang, D. Chen, W. Huang, N. Yang, Q. Yuan and Y. Yang, *Exploration*, 2023, **3**, 20210027.
30 D. K. Ban, T. Bodily, A. G. Karkisaval, Y. Dong, S. Natani, A. Ramanathan, A. Ramil, S. Srivastava, P. Bandaru and G. Glinsky, *Proc. Natl. Acad. Sci. U. S. A.*, 2022, **119**, e2206521119.

Published on 23 d'agost 2025. Downloaded on 7/2/2026 16:13:18.

31 C. Zhao, T. Man, Y. Cao, P. S. Weiss, H. G. Monbouquette and A. M. Andrews, *ACS Sens.*, 2022, **7**, 3644–3653.
32 B. Xiao, T. Li, X. Cao, Y. Zhang, J. He, M. Xiao and Z. Zhang, *Adv. Sci.*, 2025, e04497.
33 H. Wang, S. Hou, W. Feng, D. Li, J. Liu, W. Yang, S. Huang, F. Li, X. Zhao and F. Chen, *Mater. Today Nano*, 2025, **29**, 100565.
34 S. Hung and Y. Lee, *Biosensors*, 2025, **15**, 285.
35 A. Anand, F. Su, T. Chen, Y. Chen and Y. Chen, *ACS Sens.*, 2025, 4095–4104.
36 H. Alvandi, F. Asadi, A. H. Rezayan, H. Hajghassem and F. Rahimi, *Anal. Chim. Acta*, 2025, 343816.
37 M. Salehirozveh, R. Bonné, P. Kumar, F. Abazar, P. Dehghani, I. Mijakovic and V. A. Roy, *Nanoscale*, 2025, 4543–4555.
38 K. A. Yusof, R. Abdul Rahman, M. A. Zulkefle, S. H. Herman and W. F. H. Abdullah, *J. Sens.*, 2016, **2016**, 7594531.
39 J. An, H. Park, J. Kim, H. Park, T. Kim, C. Park, J. Kim, M. Lee and T. Lee, *ACS Sens.*, 2023, **8**, 3174–3186.
40 A. Purwidyantri, L. Kamajaya, C. Chen, J. Luo, C. Chiou, Y. Tian, C. Lin, C. Yang and C. Lai, *J. Electrochem. Soc.*, 2018, **165**, H3170.
41 T. Pan, C. Wang, W. Weng, C. Lai, Y. Lu, C. Wang, I. Hsieh and M. Wen, *Biosens. Bioelectron.*, 2022, **201**, 113977.
42 Z. Rahmati and M. Roushani, *Microchim. Acta*, 2022, **189**, 287.
43 N. A. Lidiawati, M. F. Raihan, A. Hermawan, O. Floweri, R. V. Manurung, M. Iqbal, A. Nuruddin, B. Yuliarto and N. L. W. Septiani, *Sens. Int.*, 2025, **6**, 100331.
44 H. Asaadi, Z. Meshkat, E. Aryan, S. B. T. Sany, H. Farsiani, J. Dorazehi, B. Hatamluyi and S. Abolbashari, *Sens. Actuators, B*, 2024, **411**, 135707.
45 P. Kanagavalli, R. A. Elkaffas and S. Eissa, *Chem. Eng. J.*, 2025, 164015.
46 P. Tan, S. Shen, Y. Zheng, Y. Tang, Y. Luo, Z. Zhang, D. Men and G. Duan, *Small*, 2025, **21**, 2407709.
47 X. Zhang, M. Liu and R. Han, *J. Environ. Chem. Eng.*, 2021, **9**, 106672.
48 C. Liu, Z. Zhang, M. Chen, H. Zhao, F. Duan, D. Chen, M. Wang, S. Zhang and M. Du, *Chem. Commun.*, 2017, **53**, 3941–3944.
49 C. Guo, F. Su, Y. Song, B. Hu, M. Wang, L. He, D. Peng and Z. Zhang, *ACS Appl. Mater. Interfaces*, 2017, **9**, 41188–41199.
50 W. Lu, Z. Wei, Z. Gu, T. Liu, J. Park, J. Park, J. Tian, M. Zhang, Q. Zhang and T. Gentle III, *Chem. Soc. Rev.*, 2014, **43**, 5561–5593.
51 X. Zhong, F. Wang, J. Piao and Y. Chen, *Analyst*, 2021, **146**, 2825–2833.
52 J. H. Cavka, S. Jakobsen, U. Olsbye, N. Guillou, C. Lamberti, S. Bordiga and K. P. Lillerud, *J. Am. Chem. Soc.*, 2008, **130**, 13850–13851.
53 M. Jang, H. Park, H. Park, Y. Yoon, S. Lee, J. Min and T. Lee, *Chem. Eng. J.*, 2024, **497**, 154806.
54 Y. Yoon, Y. Kwon, H. Park, S. Lee, C. Park and T. Lee, *BioChip J.*, 2024, **18**, 1–21.
55 Y. Yoon, C. Baek, D. Yoo, Y. Seo, S. Lee, S. W. Shin, J. Min and T. Lee, *Chem. Eng. J.*, 2024, **499**, 155898.
56 M. Ju, J. An, H. Park, Y. Seo, H. Im, H. Sohn, J. Min and T. Lee, *Microchem. J.*, 2025, 112970.
57 Y. S. Kim, N. H. A. Raston and M. B. Gu, *Biosens. Bioelectron.*, 2016, **76**, 2–19.
58 Y. Kwon, M. Lee, N. K. Kaushik, H. Y. Yoo, C. Park, M. Lee and T. Lee, *Chem. Eng. J.*, 2025, **506**, 159935.
59 N. Kwon, S. Lee, M. Jang, J. Lee, C. Park and T. Lee, *BioChip J.*, 2024, **18**, 93–102.
60 H. Park, H. Lee, M. Lee, C. Baek, J. A. Park, M. Jang, Y. Kwon, J. Min and T. Lee, *Bioconjugate Chem.*, 2023, **34**, 1486–1497.
61 S. Noh, H. Lee, J. Kim, H. Jang, J. An, C. Park, M. Lee and T. Lee, *Biosens. Bioelectron.*, 2022, **207**, 114159.
62 M. Lee, S. J. Park, G. Kim, C. Park, M. Lee, J. Ahn and T. Lee, *Biosens. Bioelectron.*, 2022, **199**, 113872.
63 N. C. Vieira, A. Figueiredo, J. F. dos Santos, S. M. Aoki, F. E. Guimarães and V. Zucolotto, *Anal. Methods*, 2014, **6**, 8882–8885.
64 D. Kwong Hong Tsang, T. J. Lieberthal, C. Watts, I. E. Dunlop, S. Ramadan, A. E. del Rio Hernandez and N. Klein, *Sci. Rep.*, 2019, **9**, 13946.
65 Y. Kutovyi, H. Hlukhova, N. Boichuk, M. Menger, A. Offenhäusser and S. Vitusevich, *Biosens. Bioelectron.*, 2020, **154**, 112053.
66 W. C. Lee, H. Lee, J. Lim and Y. J. Park, *Appl. Phys. Lett.*, 2016, **109**, 223701.
67 F. S. Nahm, *Korean J. Anesthesiol.*, 2022, **75**, 25–36.
68 N. A. Obuchowski and J. A. Bullen, *Phys. Med. Biol.*, 2018, **63**, 07TR01.
69 S. Park and T. Oh, *J. Vet. Clin.*, 2016, **33**, 97–101.
70 M. Chae, J. H. Park, H. W. Son, K. S. Hwang and T. G. Kim, *Sens. Actuators, B*, 2018, **262**, 876–883.
71 M. Chae, J. H. Park, H. W. Son, K. S. Hwang and T. G. Kim, *Sens. Actuators, B*, 2018, **262**, 876–883.
72 S. Hideshima, R. Sato, S. Kuroiwa and T. Osaka, *Biosens. Bioelectron.*, 2011, **26**, 2419–2425.
73 H. Yang and T. Sakata, *Sensors*, 2019, **19**, 3393.
74 C. Chu, I. Sarangadharan, A. Regmi, Y. Chen, C. Hsu, W. Chang, G. Lee, J. Chyi, C. Chen and S. Shiesh, *Sci. Rep.*, 2017, **7**, 5256.
75 T. Sakata, S. Matsumoto, Y. Nakajima and Y. Miyahara, *Jpn. J. Appl. Phys.*, 2005, **44**, 2860.
76 X. Xia, *Bioinformatics and the Cell: Modern Computational Approaches in Genomics, Proteomics and Transcriptomics*, 2007, 207–219.
77 N. Bhalla, A. F. Payam, A. Morelli, P. K. Sharma, R. Johnson, A. Thomson, P. Jolly and F. Canfarotta, *Sens. Actuators, B*, 2022, **365**, 131906.
78 P. Tetyana, P. M. Shumbula and Z. Njengele-Tetyana, in *Biosensors: Design, Development and ApplicationsBiosensors: Design, Development and Applications*, IntechOpen, 2021.
79 P. Dongiovanni, M. Meroni, S. Casati, R. Goldoni, D. V. Thomaz, N. S. Kehr, D. Galimberti, M. Del Fabbro and G. M. Tartaglia, *Int. J. Oral Sci.*, 2023, **15**, 27.
80 S. Kumari, M. Samara, R. Ampadi Ramachandran, S. Gosh, H. George, R. Wang, R. P. Pesavento and M. T. Mathew, *Biomed. Mater. & Devices*, 2024, **2**, 121–138.

 This journal is © The Royal Society of Chemistry 2025

81 D. Zeng, C. Wang, C. Mu, M. Su, J. Mao, J. Huang, J. Xu, L. Shao, B. Li and H. Li, *Ann. Transl. Med.*, 2021, **9**, 1080.
82 C. Osiowy, *J. Clin. Microbiol.*, 1998, **36**, 3149–3154.
83 J. C. Aguilar, M. P. Pérez-Breña, M. L. García, N. Cruz, D. D. Erdman and J. E. Echevarría, *J. Clin. Microbiol.*, 2000, **38**, 1191–1195.
84 M. E. Terlizzi, B. Massimiliano, S. Francesca, F. Sinesi, V. Rosangela, G. Stefano, C. Costa and C. Rossana, *J. Virol. Methods*, 2009, **160**, 172–177.
85 S. Cordey, Y. Thomas, P. Cherpillod, S. van Belle, C. Tapparel and L. Kaiser, *J. Virol. Methods*, 2009, **156**, 166–168.

Published on 23 d'agost 2025. Downloaded on 7/2/2026 16:13:18.